



MOF-derived Cu@Cu₂O heterogeneous electrocatalyst with moderate intermediates adsorption for highly selective reduction of CO₂ to methanol

Xian Yang, Jun Cheng^{*}, Xiao Yang, Yang Xu, Weifu Sun, Junhu Zhou

State Key Laboratory of Clean Energy Utilization, Zhejiang University, Hangzhou 310027, China

ARTICLE INFO

Keywords:

CO₂ electroreduction
Cu-BTC
Cu@Cu₂O
In-situ ATR-FTIR

ABSTRACT

To improve Faradaic efficiency (FE) of CO₂ reduction reaction (CO₂RR) to methanol over Cu-based complex electrocatalysts, a novel MOF-derived Cu@Cu₂O heterogeneous electrocatalyst with moderate intermediates adsorption was proposed for highly selective reduction of CO₂ to methanol. XRD and HRTEM confirmed the presence of a distinct heterogeneous interface between Cu and Cu₂O, while XPS verified the existence of Cu⁰/Cu⁺ and OH on catalyst surfaces. Cu⁰/Cu⁺ with a moderate CO* binding energy and OH which favored H* adsorption were conducive to hydrogenation reduction of CO₂ to methanol. The intermediate products CO*, COOH*, and CHO* were detected on in-situ electrochemical ATR-FTIR spectroscopy. The most favorable reduction route of CO₂ to methanol was as follows: CO₂ → COOH* → CO*+H₂O → CHO* → CH₂O* → CH₂OH* → CH₃OH. The FE of electrochemical CO₂ reduction to methanol over Cu@Cu₂O-400 °C electrocatalyst was ≥35% at -0.6 ~ -1.0 V (vs. RHE). The Cu@Cu₂O-400 °C electrocatalyst exhibited a peak FE_{CH₃OH} of 45% at -0.7 V, which was attributed to synergistic effect between Cu⁰ and Cu⁺ active sites.

1. Introduction

The electrocatalytic reduction of CO₂ is highly significant for the conversion of intermittent wind or solar electricity into chemical energy [1]. Among the liquid products formed upon CO₂ reduction, methanol (CH₃OH) is considered a relatively appropriate substitutive fuel for automobiles [2]. However, the inevitable hydrogen evolution reaction (HER) and poor product selectivity are challenges for electrochemical CO₂ reduction processes [3–6]. In addition, the electrochemical CO₂ reduction to methanol is a reaction of six protons coupled with six electron transfer processes [7–9], meaning it has slower reaction kinetics and that it is more difficult to produce methanol compared to the two-electron reaction that generates CO. As a result, the design of attractive electrocatalysts with high selectivity toward methanol is extremely important.

In recent years, many studies have shown that precious metals and copper-based materials are promising catalysts for electrochemical CO₂ reduction to methanol [10–12]. Among these catalysts, Cu was the only transition metal material recognized as a promising catalyst for the electrocatalytic production of hydrocarbons or alcohols [13]. However, Cu-based catalysts generally produced a wide variety of liquid products with very low selectivity toward methanol [14]. Hence, modifying the

morphology, vacancies, and oxidation state of these Cu-based catalysts were frequently employed strategies to improve their product selectivity [15–17]. In particular, Cu(I)-based catalysts had outstanding performance for the reduction of CO₂ to alcohols [18]. For example, a Cu(I) cluster crystal coordination polymer (NNU-33(H)) molecular catalyst exhibited excellent selectivity for CO₂ conversion to CH₄, with a Faradaic efficiency (FE_{CH₄}) greater than 75% due to its significant intramolecular cuprophilic interactions [19]. However, Cu(I) sites were extremely unstable in electrocatalytic reduction reactions and are easily reduced to Cu(0) sites [20]. Therefore, stabilizing these Cu(I) active sites in catalytic systems was the key to achieving the highly selective reduction of CO₂ to methanol. Specifically, strong Cu-Cu coordination could effectively stabilize Cu(I) active sites and increase catalyst conductivity [21]. For example, Gong and co-workers described the introduction of metallic Cu nanoparticle on Cu₂O films to achieve CH₃OH generation with a FE of 53.6% in a photo-electrocatalytic cell [22]. However, the poor conductivity of semiconductor Cu₂O thin films was not suitable for electrocatalytic reduction of CO₂, and the Cu nanoparticles loaded on Cu₂O films by e-beam evaporation were not uniform, Cu/Cu₂O interfaces were extremely unstable. Thus, the design of a heterostructure electrocatalyst containing stable Cu(0)/Cu(I) interface is necessary to achieve the highly selective electrocatalytic reduction of

^{*} Corresponding author.

E-mail address: juncheng@zju.edu.cn (J. Cheng).

<https://doi.org/10.1016/j.cej.2021.134171>

Received 29 September 2021; Received in revised form 4 December 2021; Accepted 11 December 2021

Available online 16 December 2021

1385-8947/© 2021 Elsevier B.V. All rights reserved.

CO₂ to methanol.

Metal-organic frameworks (MOFs) are crystalline materials formed by connecting metal ions and organic ligands through coordination bonds. MOFs have large specific surface areas and highly dispersed unsaturated metal centers that can be used as electrocatalysts [23]. MOFs had been widely used in the electrocatalytic reduction of CO₂. In particular, Cu-based MOFs (e.g., Cu-BTC) had been utilized for electrochemical CO₂ reduction to obtain liquid products [24]. Although pristine Cu-BTC had been reported to show promising performance for the electrocatalytic reduction of CO₂, its low methanol selectivity, poor electrical conductivity, and limited stability were significant limitations [25]. Therefore, to avoid these issues, metal ions in the MOF had been converted into metal clusters, metal oxides, and even metal single atoms by calcination. At the same time, the organic ligands had been carbonized into porous carbon materials, which could effectively increase conductivity and provide a large number of catalytic active sites [26].

In this work, we synthesized a new Cu@Cu₂O electrocatalyst coated with a nitrogen-doped carbon shell by calcining Cu-BTC (1,3,5-benzenetricarboxylic acid) MOFs at different temperatures in an air atmosphere. The synthesized electrocatalysts demonstrated effective performance for electrochemical CO₂ reduction to methanol. The Cu@Cu₂O-400 °C catalyst exhibited a high Faradaic efficiency (FE_{CH₃OH}) value of more than 35% from -0.6 to -1.0 V vs. RHE and its peak FE_{CH₃OH} value reached 45% at -0.7 V vs. RHE in 0.5 M KHCO₃ electrolyte. The electrocatalyst characterization results indicated that the Cu(0)/Cu(I) active sites derived from Cu-BTC moderately adsorb the CO* intermediate. In addition, the surface-adsorbed hydroxyl groups of the catalyst are also conducive to the further hydrogenation of CO* to methanol.

2. Experimental

2.1. Materials

Carbon paper (TGP-H-060) was purchased from Toray Company. Copper (II) nitrate trihydrate (Cu(NO₃)₂·3H₂O, 99%), polyvinylpyrrolidone (PVP, average mol wt. ~ 55,000), and 1,3,5-benzenetricarboxylic acid (C₉H₆O₆, 99%) were purchased from Sigma-Aldrich. Methanol (CH₃OH, for HPLC, greater than 99.99%), N,N-dimethylformamide (DMF, 99.8%), potassium bicarbonate (KHCO₃, 97%), and ethanol (C₂H₅OH, 99%) were obtained from Macklin. 5% Nafion solution and Nafion N117 proton exchange membranes were purchased from DuPont. All chemicals were directly used without further purification.

2.2. Catalyst synthesis and electrode preparation

2.2.1. Synthesis of Cu-BTC catalyst

First, 3.1 g Cu(NO₃)₂·3H₂O and 1.33 g PVP were dissolved in a 60 mL mixed solution of N,N-dimethylformamide and ethanol (V_{DMF}:V_{ethanol} = 1:1). The solution was continuously stirred for 10 min and was denoted solution A. Next, 1.47 g 1,3,5-benzenetricarboxylic acid was dissolved in a different 60 mL mixed solution of N,N-dimethylformamide and ethanol (V_{DMF}:V_{ethanol} = 1:1), which was denoted solution B. Solution B was then quickly added to solution A, and the combined solution A + B was stirred at room temperature for 30 min. Finally, solution A + B was transferred to a 200 mL Teflon-lined autoclave, and a hydrothermal reaction was performed at 120 °C for 4 h. After cooling to room temperature, the obtained blue precipitate was centrifuged and then repeatedly washed with anhydrous ethanol and deionized water to remove impurities. Afterward, the Cu-BTC catalyst was dried in a vacuum oven at 80 °C for 12 h.

2.2.2. Synthesis of Cu@Cu₂O catalyst

For the synthesis of the Cu@Cu₂O catalyst, 0.1 g Cu-BTC was transferred to a quartz crucible, which was placed in the center of a tube

furnace. The Cu-BTC was calcined for 2 h at 400 °C using a heating rate of 10 °C min⁻¹ in an air atmosphere. After cooling, the Cu@Cu₂O/NC (nitrogen-doped carbon) catalyst was obtained. For comparison, the Cu-BTC catalyst was pyrolyzed at different temperatures, denoted Cu@Cu₂O-T (where T = 300, 400, or 500 °C).

2.2.3. Electrode preparation

To prepare the cathode electrodes, 10 mg Cu@Cu₂O-T (where T = 300, 400, or 500 °C) and 100 μL Nafion solution (5 wt%) were dispersed in 1 mL isopropanol, which was ultrasonicated for at least 30 min. Next, 100 μL of the resulting homogeneous ink was coated onto a 1 × 1 cm carbon paper. Finally, the catalyst-loaded carbon paper was dried for 15 min under infrared light.

2.3. Characterization

The X-ray diffraction (XRD) patterns of the catalysts were obtained on a Bruker AXS D8 Discover powder diffractometer (Germany) using Cu-Kα radiation at 40 kV and 40 mA. The morphologies of the catalysts were observed by scanning electron microscopy (SEM, Zeiss Sigma 300, Germany) and transmission electron microscopy (TEM, FEI TalosF200x, USA). High-angle annular dark field-scanning transmission electron microscopy (HAADF-STEM) and energy-dispersive X-ray spectroscopy (EDS) were performed on an FEI Tecnai F30 (USA). X-ray photoelectron spectroscopy (XPS) was used to investigate the surface chemical environment of the catalysts with a Thermo Scientific K-Alpha spectrometer (Thermo Scientific, USA) using Al Kα radiation. The XPS spectra were calibrated with the C 1 s peak at 284.6 eV. The pore size and specific surface areas (Brunauer-Emmett-Teller, BET) of the Cu@Cu₂O catalysts were measured on an Autosorb IQ3 (Quantachrome Instruments, USA). Fourier-transform infrared spectrometry (FT-IR, Thermo Scientific Nicolet 10) and Raman spectroscopy (Thermo Fischer DXR, λ_{exc} = 633 nm) were used to analyze the surface functional groups and the graphitization degree of the catalyst.

2.4. In-situ FT-IR characterization

In-situ attenuated total reflectance infrared (ATR-IR) tests were carried out on a Nicolet Is50 FT-IR spectrometer with an MCT detector cooled by liquid nitrogen and a Pike Technologies VeeMAX III ATR accessory (Thermo Scientific, USA). The catalyst ink was coated onto a prepared polycrystalline Au film. A Pt foil and saturated Ag/AgCl were used as the counter electrode and reference electrode, respectively. 0.5 M KHCO₃ aqueous solution was used as the electrolyte, which was constantly purged with high-purity CO₂ gas (25 mL/min) during the reaction. Electrochemical measurements were obtained on a CHI 660E electrochemical workstation. The background spectrum was collected without applied potential. During the in-situ ATR-IR tests, the potential was gradually increased from -0.2 to -1.2 V vs. RHE. All ATR-IR spectra were acquired at 4 cm⁻¹ resolution and with 32 scans.

2.5. CO₂ electrochemical reduction measurements

A gas-tight H-cell separated by a Nafion N117 proton exchange membrane was used to test the performance of the catalysts for the electrochemical CO₂ reduction reaction (CO₂RR). All electrocatalytic activity measurements were carried out on an electrochemical workstation (Ivium IviumStat, Netherlands). A Pt mesh (1 × 1 cm) and saturated Ag/AgCl were utilized as the counter electrode and reference electrode, respectively. Both the cathode and anode compartments contained 15 mL 0.5 M KHCO₃ electrolyte. During each CO₂RR test, high-purity CO₂ gas was continuously pumped into the electrolyte (25 mL/min).

The gas products were detected in real time by gas chromatography (GC, 7890 Agilent) every 12 min. The liquid products were collected after the electrolysis reaction proceeded for 2 h. 0.4 mL electrolyte was

tested by ^1H NMR spectroscopy (Bruker Avance NEO 600), and 0.1 mL dimethyl sulfoxide (DMSO) was used as the internal standard. All electrochemical measurements were conducted on an electrochemical workstation (Ivium IviumStat, Netherlands). All potentials were converted into reversible hydrogen electrodes (RHE): $E_{\text{RHE}} = E_{\text{Hg}/\text{HgO}} + 0.098 + 0.059 \times \text{pH}$.

3. Results and discussion

3.1. Catalyst characterization

The carbon-supported $\text{Cu}@/\text{Cu}_2\text{O}$ -T ($T = 300, 400, \text{ and } 500\text{ }^\circ\text{C}$) catalysts were synthesized by annealing the PVP-modified Cu-BTC. First, Cu-BTC was prepared by hydrothermal method. Then, the PVP-modified Cu-BTC was calcined at various temperatures in an air atmosphere. During the pyrolysis process, the surface groups of the Cu-BTC MOF decomposed to form $\text{Cu}@/\text{Cu}_2\text{O}$ species.

The morphologies of the catalysts were characterized by scanning electron microscopy (SEM). As shown in Fig. 1, the precursor Cu-BTC has a well-defined octahedral morphology with an average diameter of 700 nm. PVP regulates the size of Cu-BTC in the hydrothermal reaction, which is the key to obtaining uniform octahedral Cu-BTC nanoparticles [27]. After calcination under air, a new type of $\text{Cu}@/\text{Cu}_2\text{O}$ electrocatalyst coated with a nitrogen-doped carbon shell was synthesized. After pyrolysis, the $\text{Cu}@/\text{Cu}_2\text{O}$ samples still show the original octahedral morphology, but their surface is now rough and porous. The average particle diameter of the $\text{Cu}@/\text{Cu}_2\text{O}$ samples is also reduced to 400–500 nm. This can be attributed to the collapse of Cu-BTC during the pyrolysis process.

To verify the Cu and Cu_2O heterostructure, TEM and HRTEM were used to characterize the morphology of the interface. As shown in Fig. 2 (a-c), the TEM images of the $\text{Cu}@/\text{Cu}_2\text{O}$ -400 $^\circ\text{C}$ catalyst exhibit a clear $\text{Cu}@/\text{Cu}_2\text{O}$ /NC core-shell structure. The average diameter of the synthesized $\text{Cu}@/\text{Cu}_2\text{O}$ nanoparticles is 120 nm. The selected area electron diffraction (SAED) pattern demonstrates the polycrystalline structure of the synthesized $\text{Cu}@/\text{Cu}_2\text{O}$ -400 $^\circ\text{C}$. The HRTEM images shown in Fig. 2 (d-f) also confirm the presence of a distinct heterogeneous interface in

$\text{Cu}@/\text{Cu}_2\text{O}$ -400 $^\circ\text{C}$. In addition, the HRTEM image shown in Fig. 2(d) explicitly shows the existence of the core-shell structure. The surface porous carbon shell inhibits the aggregation of nanoparticles and can promote the adsorption of CO_2 by lowering the energy barrier of the CO_2 reduction reaction. Fig. 2(e) and 2(f) show a lattice spacing of 0.209 nm that corresponds to the (111) crystalline plane of metallic Cu and a lattice spacing of 0.246 nm that corresponds to the (111) crystalline plane of Cu_2O , respectively. These results prove the formation of the $\text{Cu}@/\text{Cu}_2\text{O}$ heterostructure. HAADF-STEM and corresponding energy-dispersive X-ray spectra (EDS) elemental mapping images (Fig. 2(g)) were used to analyze the elemental distribution of the sample. The EDS results indicate that Cu, C, N, and O are homogeneously distributed in the $\text{Cu}@/\text{Cu}_2\text{O}$ -400 $^\circ\text{C}$ nanoparticles.

X-ray diffraction (XRD) was conducted to further confirm the existence of the Cu and Cu_2O crystal phases. Fig. 3(a) displays the XRD patterns of Cu-BTC and $\text{Cu}@/\text{Cu}_2\text{O}$ -400 $^\circ\text{C}$. The peaks observed at $2\theta = 29.6^\circ, 36.5^\circ, 42.4^\circ, 61.5^\circ, \text{ and } 73.7^\circ$ correspond to the (110), (111), (200), (220), and (311) crystal planes of Cu_2O (PDF#65-3288). In addition, the peaks at $2\theta = 43.3^\circ, 50.5^\circ, \text{ and } 74.2^\circ$ correspond to the (110), (200), and (220) planes of Cu, respectively (PDF#65-9026). Fig. 3(b) shows the XRD patterns of the $\text{Cu}@/\text{Cu}_2\text{O}$ samples calcined at different temperatures. These $\text{Cu}@/\text{Cu}_2\text{O}$ composites exhibit similar crystal phases, but as the calcination temperature increases from 300 to 500 $^\circ\text{C}$, the characteristic peaks of Cu become significantly more intense. These XRD results indicate that increasing the calcination temperature is conducive to the crystallization of copper [28].

The pore size and BET specific surface area of the catalysts were investigated by N_2 adsorption-desorption isotherms. As shown in Fig. 4, the BET specific surface areas of the original Cu-BTC and the $\text{Cu}@/\text{Cu}_2\text{O}$ samples calcined at 300, 400, and 500 $^\circ\text{C}$ are 1086, 30.7, 71.4, and 105.6 m^2/g , respectively. Moreover, the average pore diameters of Cu-BTC and the $\text{Cu}@/\text{Cu}_2\text{O}$ samples calcined at 300, 400, and 500 $^\circ\text{C}$ are 3.41, 16.85, 12.0, and 11.9 nm, respectively. This indicates that a higher degree of mesoporosity is achieved at higher carbonization temperatures. The BET surface areas of the $\text{Cu}@/\text{Cu}_2\text{O}$ samples are much smaller than those of Cu-BTC, although surface area increases with increasing calcination temperature. This may be due to the destruction of the Cu-

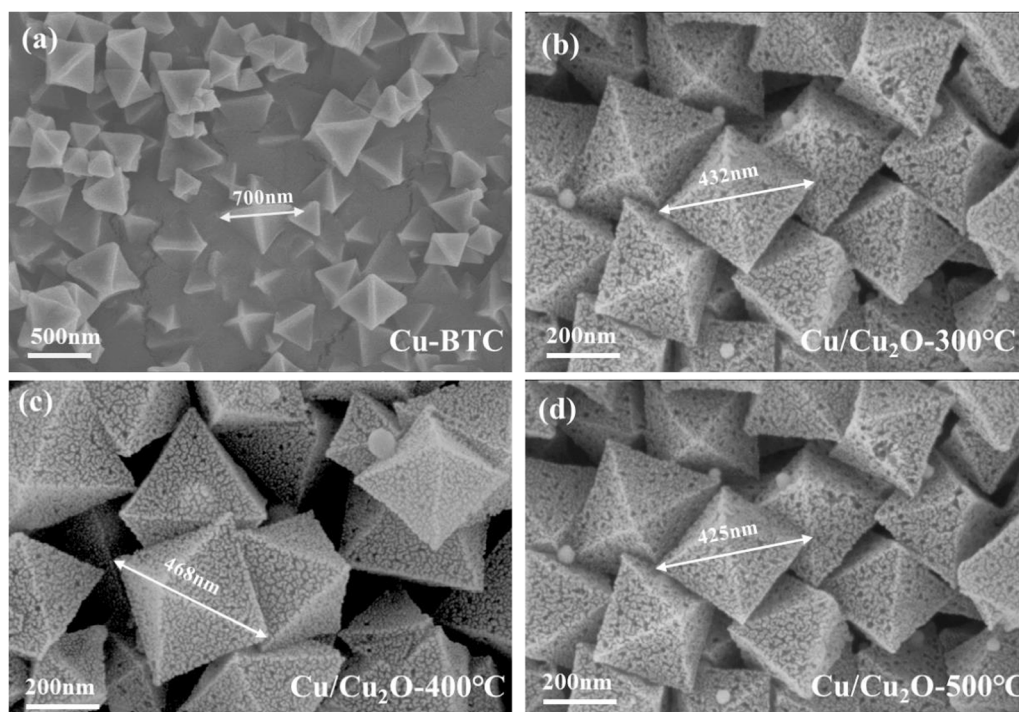


Fig. 1. SEM images of (a) Cu-BTC and $\text{Cu}@/\text{Cu}_2\text{O}$ electrocatalysts derived from Cu-BTC pyrolysis at (b) 300 $^\circ\text{C}$, (c) 400 $^\circ\text{C}$, and (d) 500 $^\circ\text{C}$.

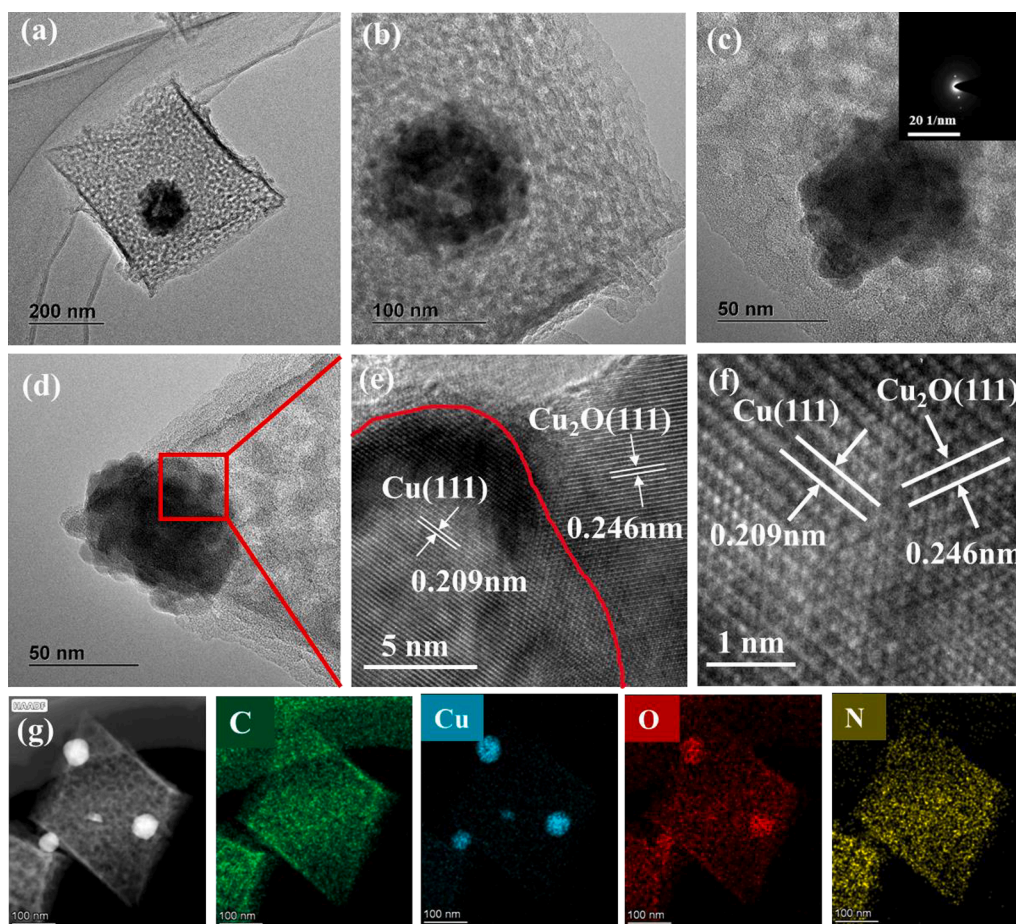


Fig. 2. (a-f) TEM and HRTEM images of Cu@Cu₂O-400 °C. (g) HAADF-STEM image and EDS elemental mapping images of Cu@Cu₂O-400 °C.

BTC structure during the calcination process, resulting in a large number of blocked or broken pores [29].

FT-IR and Raman spectra were used to analyze the surface functional groups of the catalysts. As shown in Fig. 5(a), the FT-IR pattern of Cu-BTC is consistent with those of a previous report [30]. The FT-IR peaks at 760 and 730 cm⁻¹ correspond to the bending vibrations of the C-H bond [31]. The peaks located at 1630/1560 cm⁻¹ and 1444/1371 cm⁻¹ are attributed to the asymmetric and symmetric contraction vibration peaks of the carboxylic group (-COO⁻) [30]. After calcining Cu-BTC, the original characteristic peaks at 1200–1700 cm⁻¹ almost completely disappear. A new broad peak located at about 1620 cm⁻¹ appears, corresponding to the C = C bonds of graphitic domains. Another peak at 600 cm⁻¹ is attributed to the Cu-O bond of Cu₂O [32]. Fig. 5(b) shows the Raman spectra of Cu-BTC and Cu@Cu₂O-400 °C. The peaks at 1336 and 1588 cm⁻¹ in the Raman spectra represent the D-band and G-band of graphite. In general, the relative strength of the D-band reflects the disorder degree of the crystal structure, and that of the G-band indicates the sp² bond structure of carbon. The ratio of these two peaks (I_D/I_G) is positively correlated with the presence of carbon defects [33]. The I_D/I_G value of Cu@Cu₂O-400 °C is 0.95, higher than the 0.67 I_D/I_G value of Cu-BTC. This indicates that the calcined catalyst has more surface carbon defects. It has been reported that surface defects are beneficial for the electrocatalytic reduction of CO₂.

XPS analysis was conducted to further confirm the composition and chemical state of the surface elements of the Cu@Cu₂O samples after different calcination temperatures. The wide-scan XPS spectrum of Cu@Cu₂O-400 °C shows that Cu, C, N, and O are uniformly distributed on the catalyst surface, consistent with the EDS results (Fig. 2(g)). As shown in Fig. 6(a), the high-resolution XPS Cu 2p spectra show two main peaks, the Cu 2p_{3/2} peak located at 932.3 eV and the Cu 2p_{1/2} peak

located at 952.5 eV. The binding energies of these two main peaks indicate that they can be assigned to Cu⁺ or Cu⁰ species [34]. Two weak satellite peaks are also observed at 943.5 eV and 962 eV, indicating the existence of CuO. This might be due to the oxidation of some of the Cu₂O to CuO during calcination in air [35]. To characterize the Cu⁰ and Cu⁺, the Cu LMM X-ray-induced Auger peaks were also measured. As shown in Fig. 6(b), the fitted peaks at 570.2 eV and 572.5 eV are the characteristic peaks of Cu⁰ and Cu⁺, while the other two peaks are the transition state peaks of the Cu LMN spectra [36]. As shown in Table S1, the total copper content of the catalysts did not significantly change with increasing calcination temperature. However, the composition of Cu oxidation states did change with different calcination temperatures. The Cu⁰ ratio significantly increased, while the Cu⁺ ratio was the highest in the Cu@Cu₂O-400 °C sample. This is potentially because Cu is oxidized to Cu₂O in air under high-temperature calcination. However, with increasing calcination temperature, Cu₂O easily oxidizes to CuO. [35]. Therefore, 400 °C is the optimal calcination temperature for achieving the highest level of Cu⁺. Cu⁺ has a strong adsorption effect on CO* and can promote the formation of the intermediate product CHO*, which is beneficial for electrocatalytically reducing CO₂ to CH₃OH. Previous studies have also confirmed that the synergistic effect of Cu⁰ and Cu⁺ can effectively promote the production of alcohols.

The O 1 s XPS spectra (Fig. 6(c)) show three fitted peaks. The peak located at 530 eV is attributed to Cu-O, while the peak at 531.05 eV is assigned to C = O. The peak at 532.8 eV is ascribed to O-H on the catalyst surface [37]. The oxygen content of the samples calcined at different temperatures is shown in Fig. S3. The OH peak proportion (30.5%) of the Cu@Cu₂O-400 °C catalyst is higher than that of Cu@Cu₂O-300 °C (24.8%) and Cu@Cu₂O-500 °C (27.8%). In the CO₂RR process, OH species interact with CO* to form stable carbonyl groups,

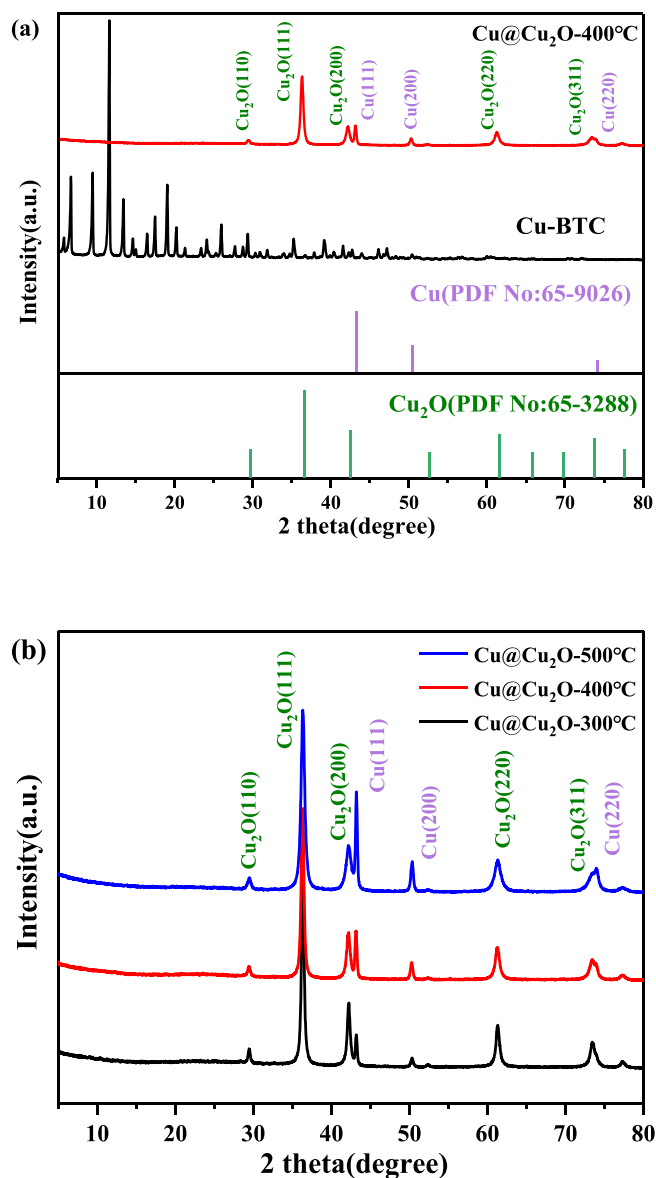


Fig. 3. (a) XRD patterns of Cu-BTC and Cu@Cu₂O-400 °C. (b) XRD patterns of Cu@Cu₂O electrocatalysts derived from Cu-BTC pyrolysis at 300 °C, 400 °C, and 500 °C.

which both protect the oxygen from being protonated and occupy the valence electrons of C to avoid the formation of C = C bonds (thus avoiding the formation of C₂H₄) [38]. The high-resolution N 1s spectra and nitrogen content of the Cu@Cu₂O samples calcined at different temperatures are displayed in Fig. S1 and Table S1. The N 1s peaks can be deconvoluted into four peaks at 398.3, 399.0, 400.3, and 401.3 eV, which are respectively assigned to pyridinic N, pyrrolic N, graphitic N, and oxidized N. The concentration of pyridinic N decreased from 56.5% to 44.05% and the concentration of graphitic N increased from 5% to 16.7% with increasing calcination temperature from 300 to 500 °C. This might be due to the decomposition of unstable pyridine N to the more stable graphite N at high temperatures [39].

3.2. CO₂ electrocatalytic reduction

The Cu@Cu₂O catalysts calcined at 300, 400, and 500 °C were tested in the electrocatalytic reduction of CO₂. The CO₂RR tests of the Cu@Cu₂O catalysts were performed in a three-electrode system with saturated 0.5 M KHCO₃. Linear sweep voltammetry (LSV) plots were

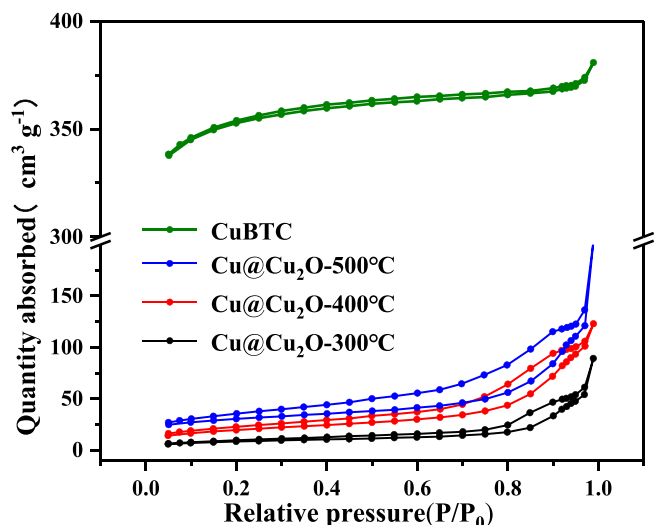


Fig. 4. N₂ adsorption–desorption isotherms of Cu-BTC and Cu@Cu₂O electrocatalysts derived from Cu-BTC pyrolysis at 300 °C, 400 °C, and 500 °C.

obtained to determine the current density of the samples, as shown in Fig. 7(a). The LSV plots show that the Cu@Cu₂O-400 °C catalyst exhibits the highest current density in the potential range of –0.6 to –1.0 V (vs. RHE) compared to the Cu@Cu₂O-300 °C and Cu@Cu₂O-500 °C samples. This indicates that Cu@Cu₂O-400 °C has faster electron transfer and better performance for CO₂RR [40]. The CO₂ reduction gas and liquid products were detected by on-line GC and ¹H NMR after conducting potentiostatic electrolysis for 2 h. As shown in Fig. 7(b-d), the CO₂RR tests resulted in three products: H₂, CO, and CH₃OH. The FE_{CH₃OH} of Cu@Cu₂O-400 °C is higher than that of the other catalysts (Fig. 7(e)). Cu@Cu₂O-400 °C has a high FE_{CH₃OH} of more than 35% from –0.6 to –1.0 V vs. RHE, reaching a maximum FE_{CH₃OH} value of 45% at –0.7 V vs. RHE in the 0.5 M KHCO₃ electrolyte. In comparison, Cu@Cu₂O-300 °C exhibits a low maximum FE_{CH₃OH} value of 26.5% at –0.6 V vs. RHE and Cu@Cu₂O-500 °C reaches a maximum FE_{CH₃OH} value of 40% at –0.7 V vs. RHE. Due to the abundant mixed active sites of Cu⁺ and Cu⁰, the synthesized Cu@Cu₂O-400 °C was considered to be an effective and highly selective catalyst. According to the XRD and XPS analysis, the relative content ratio of Cu⁺/Cu⁰ changes with increasing calcination temperature. As shown in Table S1 and Fig. S2, the Cu⁺/Cu⁰ ratio of Cu@Cu₂O-400 °C is 0.84, which is much higher than that of Cu@Cu₂O-300 °C (0.42) and Cu@Cu₂O-500 °C (0.57). Therefore, these CO₂RR results indicate that the abundant Cu⁺ species in Cu@Cu₂O-400 °C are the catalytic active sites for the synthesis of methanol by CO₂RR.

The stability of the Cu@Cu₂O-400 °C catalyst in the electrocatalytic reduction of CO₂ to methanol was studied by chronoamperometry. As shown in Fig. 7(f), the current density only slightly increased after continuous reaction for 10 h, with the value of FE_{CH₃OH} stable at about 42%. This excellent stability indicates that the carbon shell derived from Cu-BTC protects the Cu⁺/Cu⁰ heterostructure and ensures the high efficiency of this catalyst during electrocatalytic reduction.

To investigate the intrinsic activity of the Cu@Cu₂O catalysts for the effective reduction of CO₂, their electrochemically active surface areas (ECSAs) were calculated by measuring the CV curves of different sweep rates based on the double-layer capacitance (C_{dl}) theory. As shown in Fig. S4 and Fig. 8(a), the catalyst was scanned at different scanning speeds (20 mV–100 mV/s) in the voltage range of –0.3 ~ –0.1 V (vs. RHE). Referring to the CV curves in Fig. S4, the corresponding current density difference Δj at –0.2 V (vs. RHE) was selected to draw the curve, and the slope is calculated to obtain C_{dl}. The C_{dl} of Cu@Cu₂O-400 °C (11.65 mF cm^{–2}) is much higher than that of Cu@Cu₂O-300 °C (7.69 mF cm^{–2}) and Cu@Cu₂O-500 °C (4.23 mF cm^{–2}). This shows that Cu@Cu₂O-400 °C has the largest ECSA of these samples, exposing more

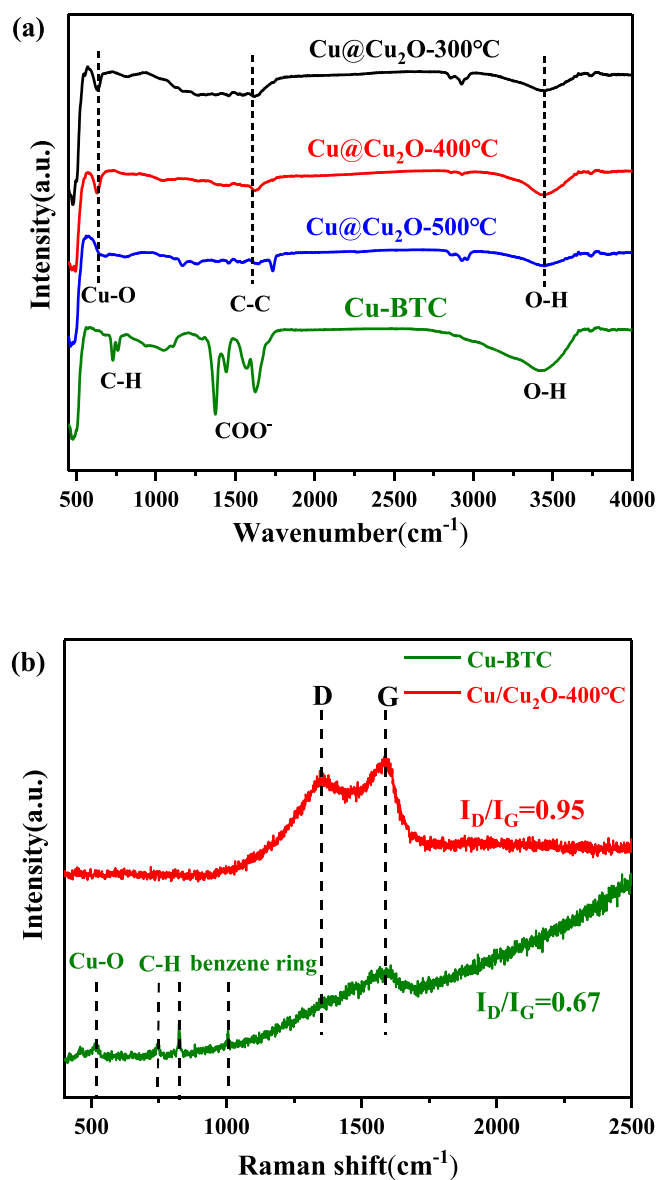


Fig. 5. (a) FTIR spectra of Cu-BTC and Cu@Cu₂O-T (T = 300, 400, and 500 °C). (b) Raman spectra of Cu-BTC and Cu@Cu₂O-400 °C.

active sites for the electrocatalytic reduction of CO₂ [41]. Electrochemical impedance spectroscopy (EIS) can also be used to further study the CO₂RR reaction kinetics of these catalysts. The Nyquist plots of the three calcined catalysts are shown in Fig. 8(b). The semicircle diameter in the Nyquist plots represents the charge transfer resistance (R_{ct}) in the reaction process. The R_{ct} of Cu@Cu₂O-400 °C (1.3 Ω) is significantly lower than the corresponding R_{ct} values of Cu@Cu₂O-300 °C (5.5 Ω) and Cu@Cu₂O-500 °C (10.8 Ω). These Nyquist plot results indicate that Cu@Cu₂O-400 °C exhibits faster mass transfer and surface electron transfer behavior during CO₂RR. This further promotes the activity of the electrocatalytic reaction and accelerates the reaction kinetics. To further verify the redox peaks of electrochemical CO₂ reduction to methanol, cyclic voltammetry (CV) tests were performed using a three-electrode cell, as shown in Fig. S6. The first reduction peak is observed at -0.2 V, which is attributed to a peak from the reduction of CO₂ to CO. In addition, a new reduction peak is observed at -0.5 V, which is attributed to hydrogenation reduction of CO₂ to methanol.

In-situ ATR-IR measurements were carried out to detect the intermediates generated during CO₂RR. As illustrated in Fig. 9 (a-b), in-situ ATR-FTIR spectra of the Cu@Cu₂O-400 °C catalyst were collected

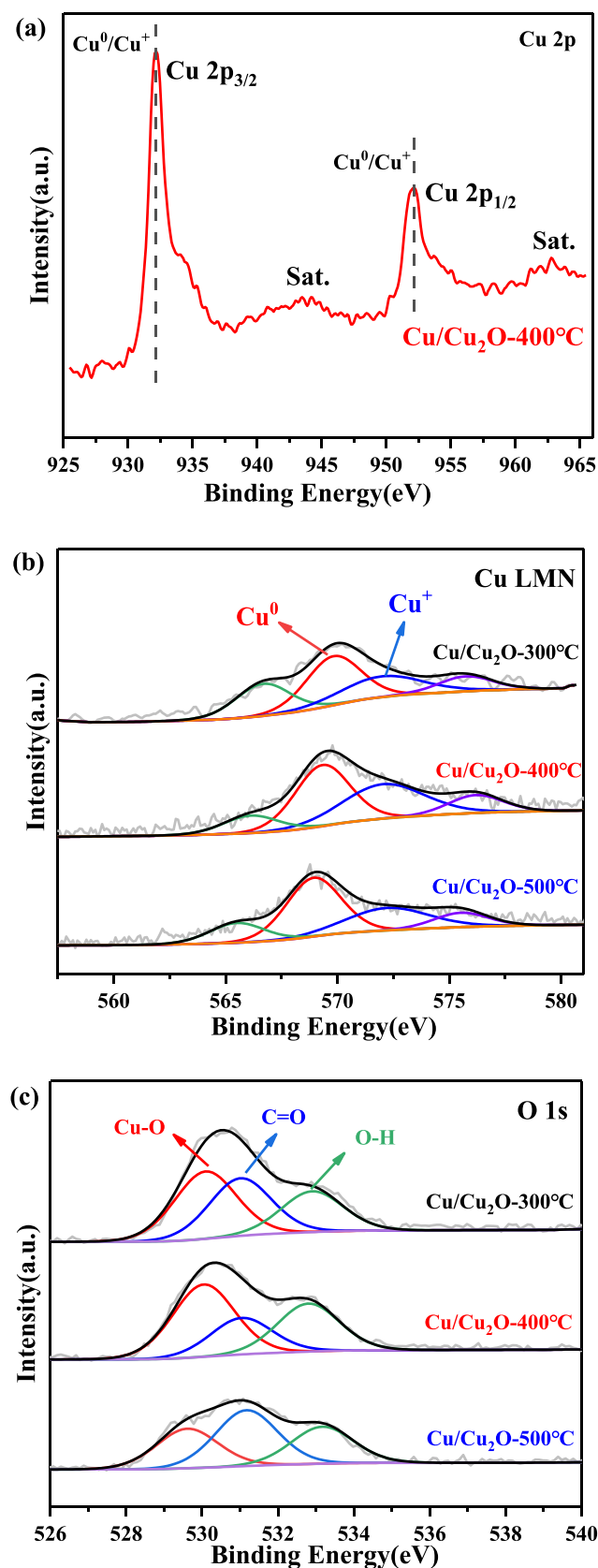


Fig. 6. (a) High-resolution Cu 2p XPS spectrum of Cu@Cu₂O-400 °C. (b) High-resolution Cu LMN and (c) O 1s XPS spectra of Cu@Cu₂O-T (T = 300, 400, and 500 °C).

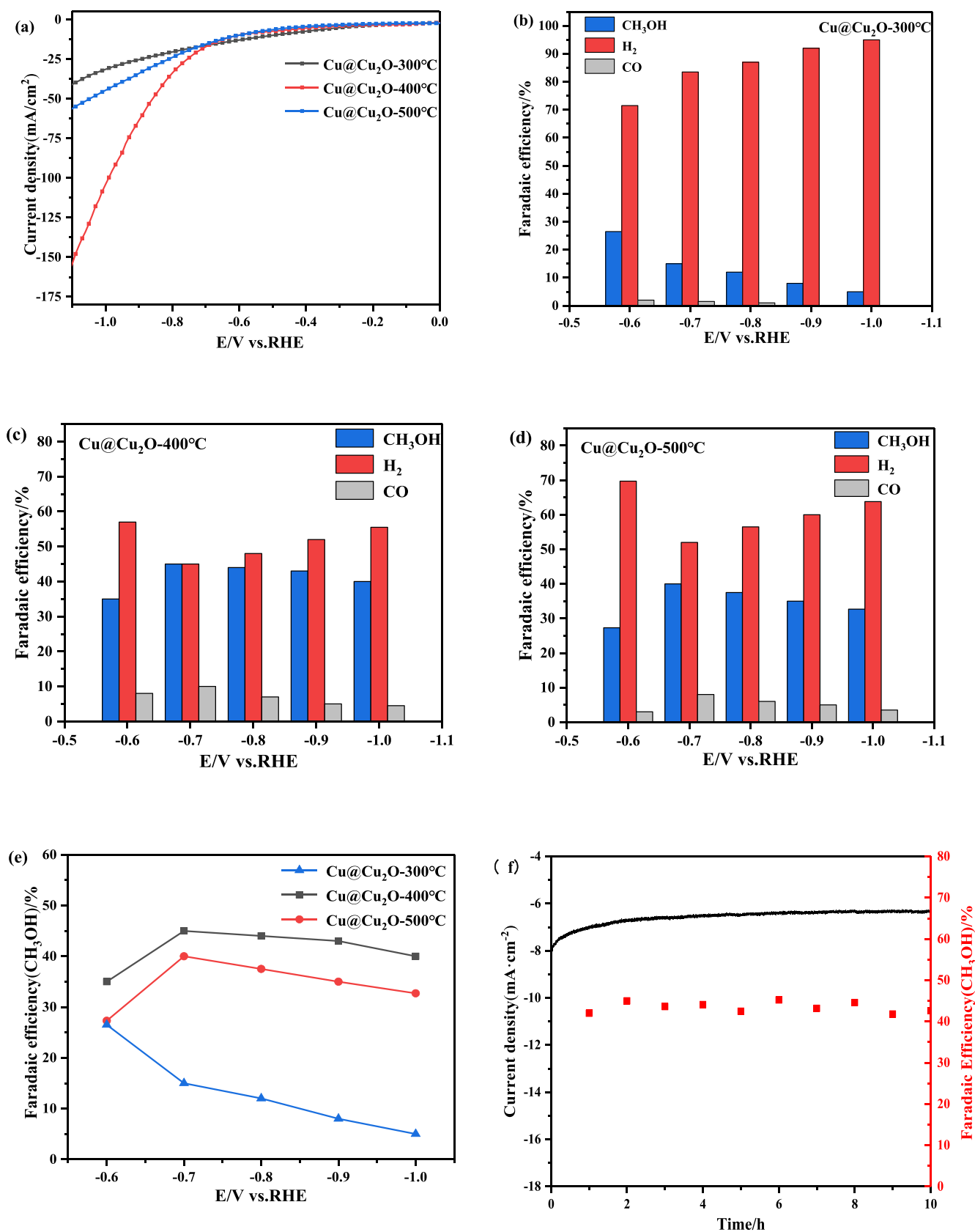


Fig. 7. (a) LSV curves of Cu@Cu₂O-T electrocatalysts (T = 300, 400, and 500 °C) measured in CO₂-saturated 0.5 M KHCO₃. Faradaic efficiencies of (b-d) all products and (e) CH₃OH over Cu@Cu₂O-T electrocatalysts at various applied potentials in CO₂-saturated 0.5 M KHCO₃. (f) Stability of Cu@Cu₂O-400 °C during CO₂ electrochemical reduction.

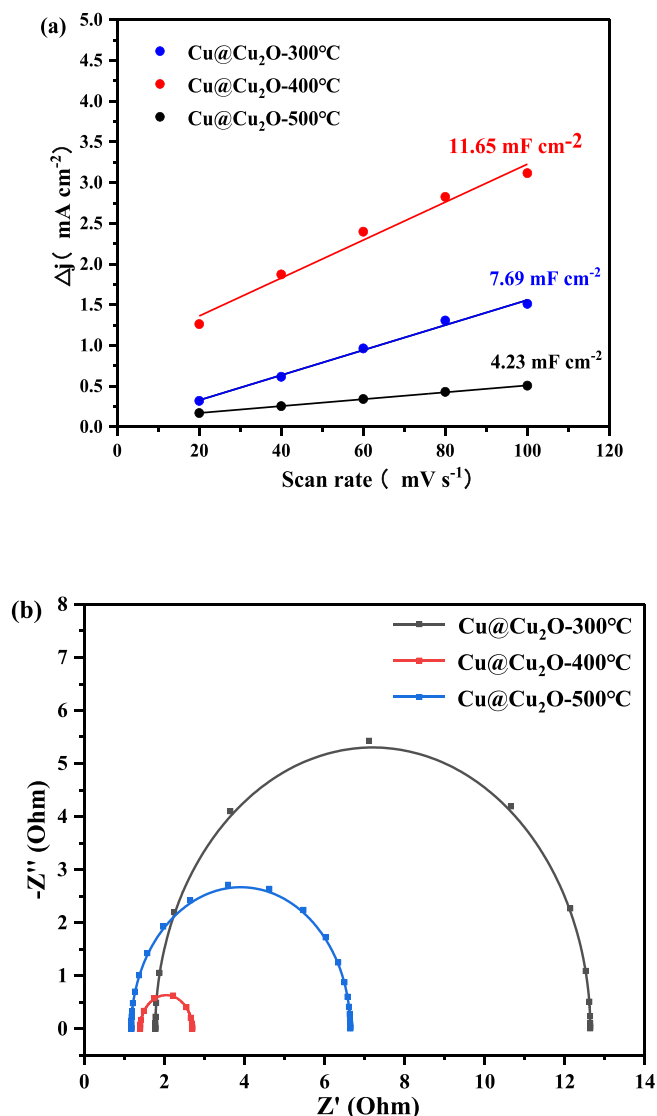


Fig. 8. (a) Electrochemical active surface area, (b) Nyquist plots (at -0.8 V vs. RHE) of Cu@Cu₂O-T (T = 300, 400, and 500 °C) electrocatalysts.

from -0.6 to -0.9 V vs. RHE, and each spectrum was acquired after 32 continuous scans. As can be seen, the characteristic band located at 2350 cm^{-1} is ascribed to the adsorption of CO₂ [42]. The catalyst exhibits the highest CO₂ peak intensity at -0.7 V vs. RHE, consistent with the CO₂RR experimental results. The peak located at 1690 cm^{-1} is potentially the characteristic peak of HCO₃* [43]. Two new characteristic peaks located at 1390 and 2065 cm^{-1} can also be observed, and these are attributed to COOH* and CO* groups [44,45]. Moreover, both peak intensities gradually increase with increasing potential from -0.6 V to -0.9 V due to the constant consumption of CO₂ during the electrocatalytic reaction. Most importantly, a new band at about 1750 cm^{-1} is ascribed to the presence of CHO*, a key intermediate for the electrocatalytic reduction of CO₂ to methanol [46]. And as the potential increased over Cu@Cu₂O-400 °C catalyst (Fig. 9b), the intensity of the intermediate (CHO*) rose and that of 1690 cm^{-1} (HCO₃*) decreased. Hence, we deduced that the KHCO₃ adsorbed on the surface would be balanced with the CO₂ molecules, and then CO₂ was converted to CHO*. These in-situ ATR-FTIR spectra show that the most likely reduction path of CO₂ to methanol is as follows:

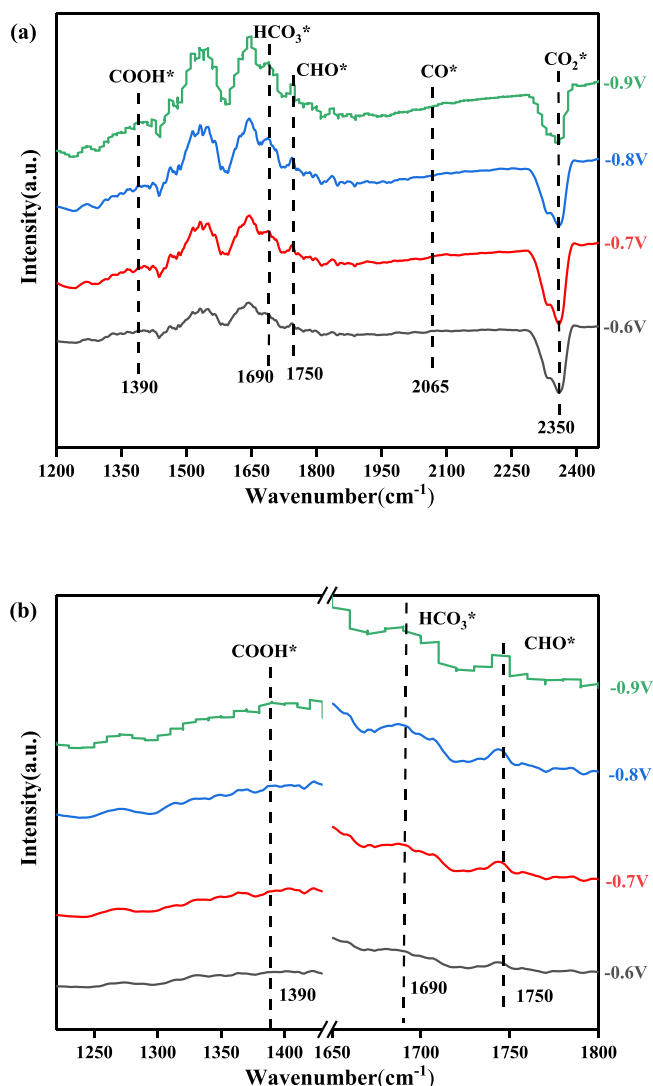
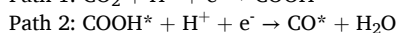
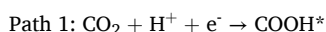
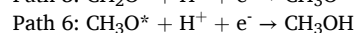
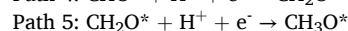
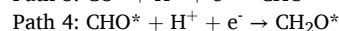


Fig. 9. (a-b) ATR-FTIR spectra of Cu@Cu₂O-400 °C at various applied potentials in CO₂-saturated 0.5 M KHCO₃.



where the asterisk represents the catalytic active site. This reaction path is graphically shown in Scheme 1. In conclusion, these in-situ ATR-IR measurements provide experimental evidence for the reaction mechanism of CO₂ reduction to methanol.

In this paper, the Cu/Cu₂O interface had a moderate CO* binding energy and stronger adsorption strength for H* compared to the original Cu₂O surface, effectively enhancing the CH₃OH production from CO₂ reduction. Specifically, the surface OH groups of the Cu@Cu₂O-400 °C catalyst is rich, and OH groups are easier to adsorb H*. In addition, H* can not only bind to Cu⁺ but also to Cu⁰, leading to a more stable adsorption [22]. Furthermore, some studies proved that the CO* adsorbed on Cu₂O is much stronger and reduces the CO* binding strength on Cu/Cu₂O [22,47]. This work has provided a new method for the design of copper-based catalysts for high-efficiency, low-cost, and stable CH₃OH generation.

4. Conclusion

In summary, a novel Cu@Cu₂O electrocatalyst was successfully developed for the electrochemical reduction of CO₂ to methanol through a Cu-BTC calcination strategy. The obtained Cu@Cu₂O catalyst effectively enhanced the adsorption of CO₂ and promoted the formation of CH₃OH due to the synergistic effect between Cu⁰ and Cu⁺ on its surface. In particular, the optimal Cu@Cu₂O-400 °C catalyst demonstrated a high FE_{CH₃OH} value of 45% at -0.7 V vs. RHE. HAADF-STEM, XPS, and XRD results demonstrated the uniform dispersion of Cu and Cu₂O crystal phases in the catalyst. The Cu/Cu₂O interface had a moderate CO* binding energy and stronger adsorption strength for H*, effectively improving the alcohol product selectivity. In addition, in-situ ATR-IR measurements confirmed the existence of the intermediate products CO*, COOH*, and CHO* and provided experimental evidence of the potential reaction mechanism. This work provides an attractive method for the design of highly efficient heterogeneous catalysts for the selective electroreduction of CO₂.

Declaration of Competing Interest

The authors declare that they have no known competing financial interests or personal relationships that could have appeared to influence the work reported in this paper.

Acknowledgements

This research was supported by the National Natural Science Foundation, China (51676171) and the Zhejiang Provincial Key Research and Development Program, China (2020C01135).

Appendix A. Supplementary data

Supplementary data to this article can be found online at <https://doi.org/10.1016/j.cej.2021.134171>.

References

- S. Ma, M. Sadakiyo, M. Heima, R. Luo, R.T. Haasch, J.I. Gold, M. Yamauchi, P. J. Kenis, Electroreduction of carbon dioxide to hydrocarbons using bimetallic Cu-Pd catalysts with different mixing patterns, *J. Am. Chem. Soc.* 139 (2017) 47–50.
- W. Zhang, Y. Hu, L. Ma, G. Zhu, Y. Wang, X. Xue, R. Chen, S. Yang, Z. Jin, Progress and perspective of electrocatalytic CO₂ Reduction for renewable carbonaceous fuels and chemicals, *Adv Sci (Weinh)* 5 (2018) 1700275.
- F.-Y. Gao, S.-J. Hu, X.-L. Zhang, Y.-R. Zheng, H.-J. Wang, Z.-Z. Niu, P.-P. Yang, R.-C. Bao, T. Ma, Z. Dang, Y. Guan, X.-S. Zheng, X. Zheng, J.-F. Zhu, M.-R. Gao, S.-H. Yu, High-curvature transition-metal chalcogenide nanostructures with a pronounced proximity effect enable fast and selective CO₂ electroreduction, *Angew. Chem. Int. Ed. Engl.* 59 (22) (2020) 8706–8712.
- P.-P. Yang, X.-L. Zhang, F.-Y. Gao, Y.-R. Zheng, Z.-Z. Niu, X. Yu, R. Liu, Z.-Z. Wu, S. Qin, L.-P. Chi, Y. Duan, T. Ma, X.-S. Zheng, J.-F. Zhu, H.-J. Wang, M.-R. Gao, S.-H. Yu, Protecting copper oxidation state via intermediate confinement for selective CO₂ electroreduction to C₂₊ fuels, *J. Am. Chem. Soc.* 142 (13) (2020) 6400–6408.
- Z.W. Seh, J. Kibsgaard, C.F. Dickens, I. Chorkendorff, J.K. Nørskov, T.F. Jaramillo, Combining theory and experiment in electrocatalysis: Insights into materials design, *Science* 355 (2017) 4998–5010.
- X. Wang, Z. Wang, F.P. García de Arquer, C.-T. Dinh, A. Ozden, Y.C. Li, D.-H. Nam, J. Li, Y.-S. Liu, J. Wicks, Z. Chen, M. Chi, B. Chen, Y. Wang, J. Tam, J.Y. Howe, A. Proppe, P. Todorović, F. Li, T.-T. Zhuang, C.M. Gabardo, A.R. Kirmani, C. McCallum, S.-F. Hung, Y. Lum, M. Luo, Y. Min, A. Xu, C.P. O'Brien, B. Stephen, B. Sun, A.H. Ip, L.J. Richter, S.O. Kelley, D. Sinton, E.H. Sargent, Efficient electrically powered CO₂-to-ethanol via suppression of deoxygenation, *Nature, Energy* 5 (6) (2020) 478–486.
- H.-P. Yang, Y.-N. Yue, S. Qin, H. Wang, J.-X. Lu, Selective electrochemical reduction of CO₂ to different alcohol products by an organically doped alloy catalyst, *Green Chem.* 18 (11) (2016) 3216–3220.
- X. Sun, Q. Zhu, X. Kang, H. Liu, Q. Qian, Z. Zhang, B. Han, Molybdenum-Bismuth bimetallic chalcogenide nanosheets for highly efficient electrocatalytic reduction of carbon dioxide to methanol, *Angew. Chem. Int. Ed. Engl.* 55 (23) (2016) 6771–6775.
- H.-P. Yang, S. Qin, H. Wang, J.-X. Lu, Organically doped palladium: a highly efficient catalyst for electroreduction of CO₂ to methanol, *Green Chem.* 17 (2015) 5144–5148.
- K.P. Kuhl, T. Hatsukade, E.R. Cave, D.N. Abram, J. Kibsgaard, T.F. Jaramillo, Electrochemical conversion of carbon dioxide to methane and methanol on transition metal surfaces, *J. Am. Chem. Soc.* 136 (40) (2014) 14107–14113.
- L.u. Lu, X. Sun, J. Ma, D. Yang, H. Wu, B. Zhang, J. Zhang, B. Han, Highly efficient electroreduction of CO₂ to methanol on palladium-copper bimetallic aerogels, *Angew. Chem. Int. Ed. Engl.* 57 (43) (2018) 14149–14153.
- J. Albo, D. Vallejo, G. Beobide, O. Castillo, P. Castaño, A. Irabien, Copper-based metal-organic porous materials for CO₂ electrocatalytic reduction to alcohols, *ChemSusChem* 10 (6) (2017) 1100–1109.
- S. Nitopi, E. Bertheussen, S.B. Scott, X. Liu, A.K. Engstfeld, S. Horch, B. Seger, I.E. L. Stephens, K. Chan, C. Hahn, J.K. Nørskov, T.F. Jaramillo, I.B. Chorkendorff, Progress and perspectives of electrochemical CO₂ reduction on copper in aqueous electrolyte, *Chem. Rev.* 119 (12) (2019) 7610–7672.
- M. Le, M. Ren, Z. Zhang, P.T. Sprunger, R.L. Kurtz, J.C. Flake, Electrochemical reduction of CO₂ to CH₃OH at copper oxide surfaces, *J. Electrochem. Soc.* 158 (5) (2011) E45, <https://doi.org/10.1149/1.3561636>.
- G.L. De Gregorio, T. Burdyny, A. Louidice, P. Iyengar, W.A. Smith, R. Buonsanti, Facet-dependent selectivity of Cu catalysts in electrochemical CO₂ reduction at commercially viable current densities, *ACS Catal.* 10 (9) (2020) 4854–4862.
- Y. Li, F. Cui, M.B. Ross, D. Kim, Y. Sun, P. Yang, Structure-sensitive CO₂ electroreduction to hydrocarbons on ultrathin 5-fold twinned copper nanowires, *Nano Lett.* 17 (2) (2017) 1312–1317.
- S.C. Lin, C.C. Chang, S.Y. Chiu, H.T. Pai, T.Y. Liao, C.S. Hsu, W.H. Chiang, M. K. Tsai, H.M. Chen, Operando time-resolved X-ray absorption spectroscopy reveals the chemical nature enabling highly selective CO₂ reduction, *Nat. Commun.* 11 (2020) 3525.
- X. Tan, C. Yu, C. Zhao, H. Huang, X. Yao, X. Han, W. Guo, S. Cui, H. Huang, J. Qiu, Restructuring of Cu₂O to Cu₂O@Cu-metal-organic frameworks for selective electrochemical reduction of CO₂, *ACS Appl. Mater. Interfaces* 11 (10) (2019) 9904–9910.
- L. Zhang, X.-X. Li, Z.-L. Lang, Y. Liu, J. Liu, L. Yuan, W.-Y. Lu, Y.-S. Xia, L.-Z. Dong, D.-Q. Yuan, Y.-Q. Lan, Enhanced cuprophilic interactions in crystalline catalysts facilitate the highly selective electroreduction of CO₂ to CH₄, *J. Am. Chem. Soc.* 143 (10) (2021) 3808–3816.
- D. Ren, Y. Deng, A.D. Handoko, C.S. Chen, S. Malkhandi, B.S. Yeo, Selective electrochemical reduction of carbon dioxide to ethylene and ethanol on Copper(I) oxide catalysts, *ACS Catal.* 5 (5) (2015) 2814–2821.
- N.V.S. Harisomayajula, S. Makovetskiy, Y.-C. Tsai, Cuprophilic interactions in and between molecular entities, *Chemistry* 25 (38) (2019) 8936–8954.
- X. Chang, T. Wang, Z.-J. Zhao, P. Yang, J. Greeley, R. Mu, G. Zhang, Z. Gong, Z. Luo, J. Chen, Y.i. Cui, G.A. Ozin, J. Gong, Tuning Cu/Cu₂O interfaces for the reduction of carbon dioxide to methanol in aqueous solutions, *Angew. Chem. Int. Ed.* 57 (47) (2018) 15415–15419.
- Z. Liang, C. Qu, W. Guo, R. Zou, Q. Xu, Pristine metal-organic frameworks and their composites for energy storage and conversion, *Adv. Mater.* 30 (2018) 1702891.
- J. Albo, M. Perfecto-Irigaray, G. Beobide, A. Irabien, Cu/Bi metal-organic framework-based systems for an enhanced electrochemical transformation of CO₂ to alcohols, *Journal of CO₂ Utilization* 33 (2019) 157–165.
- Y. Zhao, L. Zheng, D. Jiang, W. Xia, X. Xu, Y. Yamauchi, J. Ge, J. Tang, Nanoengineering metal-organic framework-based materials for use in electrochemical CO₂ reduction reactions, *Small* 17 (2021) 2006590.
- C.S. Diercks, Y. Liu, K.E. Cordova, O.M. Yaghi, The role of reticular chemistry in the design of CO₂ reduction catalysts, *Nat. Mater.* 17 (4) (2018) 301–307.
- J. Cheng, X. Xuan, X. Yang, J. Zhou, K. Cen, Selective reduction of CO₂ to alcohol products on octahedral catalyst of carbonized Cu(BTC) doped with Pd nanoparticles in a photoelectrochemical cell, *Chem. Eng. J.* 358 (2019) 860–868.
- X. Han, X. He, L. Sun, X. Han, W. Zhan, J. Xu, X. Wang, J. Chen, Increasing effectiveness of photogenerated carriers by in situ anchoring of Cu₂O nanoparticles on a nitrogen-doped porous carbon yolk-shell cuboctahedral framework, *ACS Catal.* 8 (4) (2018) 3348–3356.
- X. Lin, S. Wang, W. Tu, Z. Hu, Z. Ding, Y. Hou, R. Xu, W. Dai, MOF-derived hierarchical hollow spheres composed of carbon-confined Ni nanoparticles for efficient CO₂ methanation, *Catalysis, Science & Technology* 9 (3) (2019) 731–738.
- C. Petit, B. Levasseur, B. Mendoza, T.J. Bandosz, Reactive adsorption of acidic gases on MOF/graphite oxide composites, *Microporous Mesoporous Mater.* 154 (2012) 107–112.
- J.B. DeCoste, G.W. Peterson, B.J. Schindler, K.L. Killops, M.A. Browe, J.J. Mahle, The effect of water adsorption on the structure of the carboxylate containing metal-organic frameworks Cu-BTC, Mg-MOF-74, and UiO-66, *J. Mater. Chem. A* 1 (38) (2013) 11922, <https://doi.org/10.1039/c3ta12497e>.
- W.-D. Oh, G. Lisak, R.D. Webster, Y.-N. Liang, A. Veksha, A. Giannis, J.G.S. Moo, J.-W. Lim, T.-T. Lim, Insights into the thermolytic transformation of lignocellulosic biomass waste to redox-active carbocatalyst: Durability of surface active sites, *Appl. Catal. B* 233 (2018) 120–129.
- X. Yang, J. Cheng, B. Fang, X. Xuan, N. Liu, X. Yang, J. Zhou, Single Ni atoms with higher positive charges induced by hydroxyls for electrocatalytic CO₂ reduction, *Nanoscale* 12 (35) (2020) 18437–18445.
- Z. Gu, N. Yang, P. Han, M. Kuang, B. Mei, Z. Jiang, J. Zhong, L. Li, G. Zheng, Oxygen vacancy tuning toward efficient electrocatalytic CO₂ reduction to C₂H₄, *Small Methods* (2018) 1800449.
- L. De Los Santos Valladares, D.H. Salinas, A.B. Dominguez, D.A. Najjarro, S. I. Khondaker, T. Mitrelias, C.H.W. Barnes, J.A. Aguiar, Y. Majima, Crystallization and electrical resistivity of Cu₂O and CuO obtained by thermal oxidation of Cu thin films on SiO₂/Si substrates, *Thin Solid Films* 520 (20) (2012) 6368–6374.
- H. Wu, H. Li, X. Zhao, Q. Liu, J. Wang, J. Xiao, S. Xie, R. Si, F. Yang, S. Miao, X. Guo, G. Wang, X. Bao, Highly doped and exposed Cu(I)-N active sites within

- graphene towards efficient oxygen reduction for zinc–air batteries, *Energy Environ. Sci.* 9 (2016) 3736–3745.
- [37] F. Wang, X. He, L. Sun, J. Chen, X. Wang, J. Xu, X. Han, Engineering an N-doped TiO₂@N-doped C butterfly-like nanostructure with long-lived photo-generated carriers for efficient photocatalytic selective amine oxidation, *J. Mater. Chem. A* 6 (5) (2018) 2091–2099.
- [38] C.-T. Dinh, T. Burdyny, M.G. Kibria, A. Seifitokaldani, C.M. Gabardo, F.P. García de Arquer, A. Kiani, J.P. Edwards, P. De Luna, O.S. Bushuyev, C. Zou, R. Quintero-Bermudez, Y. Pang, D. Sinton, E.H. Sargent, CO₂ electroreduction to ethylene via hydroxide-mediated copper catalysis at an abrupt interface, *Science* 360 (6390) (2018) 783–787.
- [39] H.-X. Zhong, J. Wang, Y.-W. Zhang, W.-L. Xu, W. Xing, D. Xu, Y.-F. Zhang, X.-b. Zhang, ZIF-8 derived graphene-based nitrogen-doped porous carbon sheets as highly efficient and durable oxygen reduction electrocatalysts, *Angew. Chem. Int. Ed. Engl.* 53 (51) (2014) 14235–14239.
- [40] X. Cui, Z. Pan, L. Zhang, H. Peng, G. Zheng, Selective etching of nitrogen-doped carbon by steam for enhanced electrochemical CO₂ Reduction, *Adv. Energy Mater.* 7 (2017) 1701456.
- [41] H. Cheng, X. Wu, X. Li, X. Nie, S. Fan, M. Feng, Z. Fan, M. Tan, Y. Chen, G. He, Construction of atomically dispersed Cu-N4 sites via engineered coordination environment for high-efficient CO₂ electroreduction, *Chem. Eng. J.* 407 (2021), 126842.
- [42] B. Innocent, D. Pasquier, F. Ropital, F. Hahn, J.M. Léger, K.B. Kokoh, FTIR spectroscopy study of the reduction of carbon dioxide on lead electrode in aqueous medium, *Appl. Catal. B* 94 (2010) 219–224.
- [43] X. Li, Y. Sun, J. Xu, Y. Shao, J.u. Wu, X. Xu, Y. Pan, H. Ju, J. Zhu, Y.i. Xie, Selective visible-light-driven photocatalytic CO₂ reduction to CH₄ mediated by atomically thin CuIn₂S₈ layers, *Nature, Energy* 4 (8) (2019) 690–699.
- [44] Z. Wu, H. Wu, W. Cai, Z. Wen, B. Jia, L. Wang, W. Jin, T. Ma, Engineering Bismuth-Tin interface in bimetallic aerogel with a 3D porous structure for highly selective electrocatalytic CO₂ Reduction to HCOOH, *Angewandte Chemie International Edition* 60 (22) (2021) 12554–12559.
- [45] F. Vigier, C. Coutanceau, F. Hahn, E.M. Belgsir, C. Lamy, On the mechanism of ethanol electro-oxidation on Pt and PtSn catalysts: electrochemical and in situ IR reflectance spectroscopy studies, *Journal of Electroanalytical Chemistry* 563 (2004) 81–89.
- [46] A. Wuttig, C. Liu, Q. Peng, M. Yaguchi, C.H. Hendon, K. Motobayashi, S. Ye, M. Osawa, Y. Surendranath, Tracking a common surface-bound intermediate during CO₂-to-fuels catalysis, *ACS Cent. Sci.* 2 (8) (2016) 522–528.
- [47] B. Eren, C. Heine, H. Bluhm, G.A. Somorjai, M. Salmeron, Catalyst chemical state during CO oxidation reaction on Cu(111) studied with ambient-pressure X-ray photoelectron spectroscopy and near edge X-ray adsorption fine structure spectroscopy, *J. Am. Chem. Soc.* 137 (34) (2015) 11186–11190.